

Thermal Conductivity of Diamond Mosaic Crystals Grown by Chemical Vapor Deposition: Thermal Resistance of Junctions

V.G. Ralchenko,^{1,2,3,*} A.V. Inyushkin^{4,†} Guoyang Shu,^{1,2} Bing Dai,¹ I.A. Karateev⁴,
A.P. Bolshakov^{1,2,3} A.A. Khomich,^{2,5} E.E. Ashkinazi,² E.V. Zavedeev,² Jiecai Han,¹ and Jiaqi Zhu¹


¹Center for Composite Materials and Structures, Harbin Institute of Technology, Harbin 150080, People's Republic of China

²A. M. Prokhorov Institute of General Physics RAS, Moscow 119991, Russia

³National Research Nuclear University MEPhI, Moscow 115409, Russia

⁴National Research Center Kurchatov Institute, Moscow 123182, Russia

⁵V. A. Kotel'nikov Institute of Radio Engineering and Electronics RAS, Fryazino 141120, Russia

 (Received 22 April 2021; revised 17 June 2021; accepted 30 June 2021; published 20 July 2021)

Large-area single-crystal “mosaic” diamond wafers, produced by homoepitaxial diamond chemical vapor deposition (CVD) on seed crystals aligned in close proximity, are of increasing interest for high-power electronic and optical applications, not least due to their extraordinary thermal properties. However, thermal conductivity might be reduced if a significant thermal-barrier resistance (TBR) forms on junctions between the single-crystal blocks of the mosaic. Here, using a steady-state longitudinal heat-flow method, we measure with a high accuracy the in-plane thermal conductivity $\kappa(T)$ in the broad temperature range of 6–410 K for a diamond mosaic crystal grown by microwave plasma CVD. At room temperature, the conductivity as high as $24.0 \pm 0.5 \text{ W cm}^{-1} \text{ K}^{-1}$ is determined within a single block, reducing by less than 2% only for $\kappa(T)$ measured across the junction due to low enough TBR of approximately $10^{-4} \text{ cm}^2 \text{ K W}^{-1}$. However, below 100 K the TBR strongly increases with the temperature decrease, resulting in a dramatic reduction of the mosaic thermal conductivity compared to that for the single-crystal block. We associate the appearance of TBR with a layer (approximately equal to $20 \mu\text{m}$ thick) of defected and stress material near the junction, as revealed with a confocal Raman mapping and transmission electron microscopy. The phonon scattering from defects in the zone around the junction strongly reduces the local thermal conductivity, as confirmed by modeling of heat transport. The observed temperature dependence $\kappa(T) \sim T^2$ of the local conductivity at $T < 83 \text{ K}$ suggests the dominance of the phonon-dislocation scattering among other scattering processes. Our results show that the diamond mosaics preserve excellent thermal properties of the constituent single-crystal blocks at room and higher temperatures, and can be effectively used in the applications where the thermal conductivity is of primary relevance.

DOI: [10.1103/PhysRevApplied.16.014049](https://doi.org/10.1103/PhysRevApplied.16.014049)

I. INTRODUCTION

Diamond, due to its superior properties like extraordinary high thermal conductivity, wide optical transparency window, high charge-carrier mobility, mechanical strength is the prospective material for electronic and optical applications [1–4]. The large-area polycrystalline diamond (PCD) wafers, which currently can be produced in diameters above 200 mm, are used particularly, as heat spreaders integrated to high-power GaN transistors [3,5,6], and graphene-on-diamond devices [7], in thin disk lasers [8], and as windows in high-power gyrotrons [9] and IR lasers [10]. The useful function of diamond in those applications

is the ability to effectively dissipate the heat, however, due to phonon scattering on grain boundaries the thermal conductivity in the PCD is inferior compared to that for single-crystal diamond (SCD) [11–15]. The measured conductivity of coarse-grain high-quality “white” PCD typically lays in the range of $19\text{--}21 \text{ W cm}^{-1} \text{ K}^{-1}$ at room temperature [12,14,16] and can approach approximately equal to $22 \text{ W cm}^{-1} \text{ K}^{-1}$ for thick ($> 500 \mu\text{m}$) wafers provided a significant part of the wafer with fine-grained bottom layer is removed [11,17], or if the measurement method probes only the large-grained side of the sample [18]. In comparison, single-crystal chemical vapor deposition (CVD) diamonds demonstrate even a higher thermal conductivity of up to approximately equal to $24 \text{ W cm}^{-1} \text{ K}^{-1}$ [19]. Also, the interior defects and the grain boundaries in PCD result in enhanced optical

*vg_ralchenko@mail.ru

†Inyushkin_AV@nrcki.ru

absorption and degradation of the potentially excellent optical properties. Therefore, the large-area SCD wafers are highly desirable to further improve the performance of diamond-based devices and components. However, the production of large size (several inches) SCD wafers still remains a challenge.

There are two principal ways to extend the SCD size to inch scale. The first one is based on heteroepitaxial growth on iridium film, that allows production of SCD wafers of approximately equal to 100 mm in diameter [20–22]. The second approach, known as “mosaic” growth, uses the overgrowth of homoepitaxial diamond by CVD on identically oriented several pieces of high-pressure-high-temperature (HPHT) synthesized diamond substrate assembled in one mosaic-tiled geometry, with following separation from the substrate [23–26]. Mosaic wafers produced on array of $10 \times 10 \text{ mm}^2$ clone substrates as large as $40 \times 60 \text{ mm}^2$ were demonstrated in Ref. [27]. While the major volume of the mosaics can be a high-quality low-stress material, the coalescence boundaries (junctions) between the blocks contain an enhanced defect concentration and stress [28–30] according to analysis with Raman spectroscopy. The defects, such as dislocations, in the junction region, are shown to degrade electronic performance of devices such as Schottky barrier diodes [29]. One may expect that the defects localized around the junctions can degrade also the *in-plane* thermal conductivity, by forming thermal barriers [due to a small relative area of the junction-affected defected zone, the decrease in conductivity perpendicular to the wafer should be negligible ($< 1\%$)]. In the case if the junction-induced thermal barrier resistance (TBR) would be significant, no advantage the diamond mosaic crystals in thermal management will have against the PCD. However, there is a lack up to now of experimental data on thermal conductivity of diamond mosaic crystals and on the TBR values due to their specific block structure, either at room temperature or in a broad temperature range.

Here, we report on highly accurate measurements of temperature dependence of *in-plane* thermal conductivity and TBR for a model simple diamond mosaic with only two SCD blocks with well-defined junction region. We demonstrate that at room temperature the TBR detrimental effect is quite small, of a few percent, but becomes significant below approximately 100 K. Therefore, we confirm expectations of the excellent thermal properties of large-area diamond mosaics needed for advanced electronic and optical applications.

The mosaic diamond can be regarded as a special case of PCD with very large grains (few millimeters) and well-aligned grain boundaries (GBs). The phonon scattering on grain boundaries of polycrystalline and nanocrystalline diamond was experimentally studied in a number of works [11–13, 15, 31–38]. Normally, the direct microscopic measurements of thermal conductivity of PCD characterize

the effect of TBR of the GB by averaging it over a large number of grains, which are different in size, orientation, and GB structure, while evaluation of the conductivity distribution across a single grain is a difficult task. Recently, Sood *et al.* [39] using spatially resolved time-domain thermoreflectance (TDTR) measurements in two-dimensional (2D) version made measurements of local thermal conductivity within few micrometers of individual GBs in boron-doped polycrystalline diamond, and observed strongly suppressed thermal transport near disordered grain boundaries (the suppression zone extending to distances of the order of $10 \mu\text{m}$ from GB). Qualitatively a similar conclusion has been derived earlier from local probing of conductivity by photothermal reflectance microscopy (but in one-dimensional version) by Hartmann *et al.* [32]. Both measurements were performed for polycrystalline films with random grain orientation at room temperatures only, and without knowledge on the defect structure of the particular GBs. In contrast, here we apply an essentially macroscopic classical method of steady-state temperature gradient to measure thermal transport across a single very long junction (a kind of GB) between single-crystal CVD diamond blocks of a mosaic sample, and characterized the defects and stress distribution around the junction. Moreover, we obtain the conductivity and TBR data not only at room temperature but also at lower and higher temperatures.

II. EXPERIMENTAL METHODS

A. Sample preparation

The mosaic diamond crystal is epitaxially grown in a microwave plasma CVD system (PLASSYS SDDR 150) in a $\text{CH}_4\text{-H}_2$ gas mixture on two $3 \times 3 \times 1 \text{ mm}^3$ Ib type HPHT diamond substrates placed in close proximity [28]. The large faces of the substrate are (100) oriented, and the side planes are (110) oriented. The diamond deposition is performed at the following conditions: substrate temperature $850 \text{ }^\circ\text{C}$, pressure 320 mbar, CH_4 content of 7%, total flow rate of 200 sccm, MW power 4.4 kW, growth time 100 h, growth rate $11 \mu\text{m/h}$. The grown layer is separated from the substrate by a laser cutting, and mechanically polished from all six sides to the surface roughness R_a of less than 4 nm as measured with an optical profilometer ZYGO NewView 5000. Finally, the CVD diamond plate of $5.4 \times 2.8 \times 0.96 \text{ mm}^3$ dimension is obtained, with a junction between the two crystals aligned perpendicular to the longer side (Fig. 1). The sample contained 2.7 ppm of paramagnetic substitutional nitrogen N_s , evaluated from optical absorption spectra in UV range as described elsewhere [40]. The presence of an absorption band at 520-nm wavelength imparted a very light pink tint to the mosaic. No visible (macroscopic) defects could be observed in the bulk or on the surface of the sample.

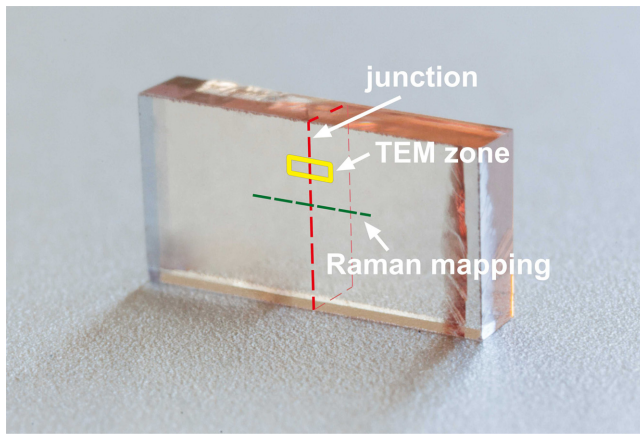


FIG. 1. Photograph of the mosaic crystal consisting of two blocks of $2.7 \times 2.8 \times 0.96 \text{ mm}^3$ each. The dashed red line marks the junction position. The rectangular yellow box shows the location on the junction line where a slice for TEM analysis is cut by FIB. Raman spectra are taken along the short green dashed line across the junction.

B. TEM characterization

To examine the diamond structure in cross section a sample for TEM is prepared in form of an approximately equal to 50-nm-thick slice by focused ion beam (FIB) technique on a scanning electron and ion microscope Helios Nanolab 600i. The TEM sample is cut exactly in the junction zone perpendicularly to the junction line, as shown in Fig. 1 to be able to compare the orientations and defect abundance on both sides of the interface between the two crystals. Firstly, the diamond surface is coated first with approximately 10-nm-thick Au film by magnetron deposition to prevent the sample charging, and then a protective 2- μm -thick Pt layer is formed locally on $15 \times 2 \mu\text{m}^2$ area by simultaneously using a Pt gas-injection system and FIB. The FIB milling with 30 keV Ga^+ ions resulted in 2- μm -wide cross sections of approximately equal to $15 \times 5 \mu\text{m}^2$, the junction located approximately in the middle of the slice. For electron transparency, the sample is thinned with 30 keV Ga^+ ions, and then with 5 keV Ga^+ ions. Final cleaning is achieved with low (2 keV) FIB milling voltage of Ga^+ ion beam to avoid a possible damage in diamond [41]. To compare the defect abundance near the junction and far away from it, another slice is cut in a location distant 30 μm from the junction. The TEM investigation is performed on a TEM and STEM Cs probe-corrected microscope Titan 80-300.

C. Raman spectroscopy

To assess the distribution of defects and stress in a zone around the junction between the crystals a confocal Raman mapping is performed in steps of 2 μm along a 400- μm path perpendicular to the junction, starting on one crystal and ending on the second block [23]. The excitation laser

beam ($\lambda = 473 \text{ nm}$) is focused on the sample top surface in a spot of approximately 1 μm , and the light from the sample is collected in backscattering geometry with microscope objective (Olympus, magnification $\times 100$, numerical aperture $\text{NA} = 0.90$). The diode-pumped solid-state laser (Nd:YAG, Laser Quantum, UK) operated in TEM00 mode with horizontal polarization of output beam is employed, the laser power of 100 mW and power density being kept constant in all measurements. The spectrum for the mosaic is measured in each location along the path. The diamond Raman peak is fit with a Lorentzian profile, and then, Raman peak position ν_R and width $\Delta\nu$ are evaluated. The diamond Raman peak position is determined with accuracy of $\pm 0.3 \text{ cm}^{-1}$ and the peak width with accuracy of $\pm 0.5 \text{ cm}^{-1}$. The deviation of peak position from the value of $\nu_{R0} = 1332.5 \text{ cm}^{-1}$ known for unstressed diamond (this is calibrated by us using a high-quality natural IIa type diamond) served to estimate the local stress [23], while the peak broadening qualitatively characterized the defect abundance.

D. Thermal conductivity measurement

The *in-plane* thermal conductivity $\kappa(T)$ is measured in the temperature range from 6 to 410 K by a heated-bar method under stationary thermal flux parallel along the longer side of the sample, as shown schematically in Fig. 2. The procedure is similar to that described elsewhere [19]. The sample is mechanically clamped to one end of a temperature-stabilized copper block (heat sink). The good thermal contact is achieved by coating both the Cu block and the sample side walls with In-Ga eutectic. A miniature resistor attached to the opposite side of the diamond plate with the IMI-7031 varnish, is the heat source. The temperature drop along the sample is measured with a battery of thin chromel-constantan thermocouples of 25 μm diameter (Omega Engineering, Inc.). The copper legs, 0.13 mm wide, of the thermocouple battery are

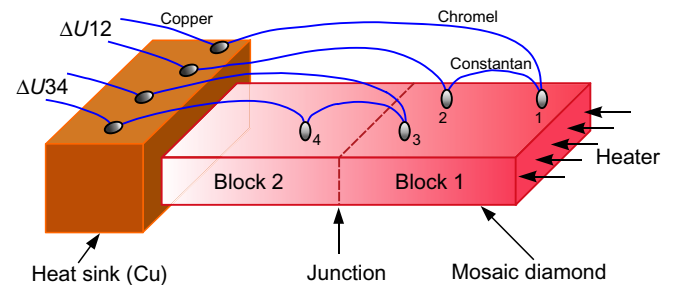


FIG. 2. Schematics of thermal conductivity measurements by a heated-bar method. The battery of thermocouples in positions 1,2 and 3,4 determines the temperature differences used to calculate the conductivity κ_{11} within the single-crystal block 1, and the conductivity κ_{12} across the junction between blocks 1 and 2, respectively.

covered with Apiezon N grease, the distance between the legs is $L = 2.5$ mm. The thermocouple sensitivity is calibrated with a pair of thermometers Cernox (Lake Shore Cryotronics, Inc.).

The thermal conductivity κ is determined according to relation $\kappa = (Q/A)/(\Delta T/L)$, where Q is heat power generated by the heater, $A = a \times b$ is the sample cross-section area, $a = 2.8$ mm and $b = 0.96$ mm being its width and thickness, and ΔT is the measured temperature difference between the “hot” and “cold” legs of the thermocouple. The measurements are carried out in vacuum, placing the sample inside a multilayer radiation shield to minimize radiation losses. The value of ΔT is very small, it ranged from below 1 mK at liquid helium temperatures to 5 mK at liquid nitrogen temperature (77 K), and further up to 50 mK at 400 K, whereas Q varied from about 0.15 mW to 80 mW through the entire T range. Note that due to extremely high thermal conductivity at low temperatures and small size of samples it is the very small ΔT to be measured that often hinders the evaluation of κ in the broad T range. The estimated error of the measured conductivity is about 2%, but at temperatures below 10–15 K it increased by several times due to two factors. (1) Decrease the sensitivity of the thermocouple: it is about $4.2 \mu\text{V/K}$ at 10 K and $2.2 \mu\text{V/K}$ at 5 K. (2) Decrease the temperature drop ΔT generated by the sample heater as the sample temperature approaches the helium-bath temperature. To reduce this error, the conductivity is measured at least 2 times at a fixed temperature [on the temperature rise and fall segments of $\kappa(T)$ curve], and up to 10 times below 6 K, then the collected data are averaged. Details of the experimental technique and error analysis are presented in Ref. [19].

For the case of thermocouples legs in positions 1 and 2 (see Fig. 2) within one crystal block, the obtained thermal conductivity κ_{11} refers to the single crystal, while for the thermocouples legs in positions 3 and 4 the heat flux crosses the junction, and the measured conductivity κ_{12} may differ from the κ_{11} due to the junction thermal resistance. The evaluation of this difference is one of the main goals of the present work. Note that when measuring the temperature dependence of thermal conductivity (κ_{11} or κ_{12}) in one experimental cycle, the battery of thermocouples is in one fixed position at all temperatures. Between experiments on $\kappa(T)$, the battery of thermocouples is moved from one position to another to measure the conductivity between its legs.

III. RESULTS AND DISCUSSION

A. Transmission electron microscopy

The results of TEM analysis of the sample cross sections within and outside the junction are presented in Fig. 3. The images in Figs. 3(a) and 3(b) correspond right to the junction region and an area approximately $30 \mu\text{m}$ away

from the junction, respectively. Numerous defects (stacking faults, twins, and dislocations) spreading from junction plane are clearly visible [Fig. 3(a)], while at the distance of $30 \mu\text{m}$ from the junction no such defects are observed [Fig. 3(b)]. These findings and the spatial variation in the defect density [Fig. 3(f)] suggest that defects observed near the interface are related to mosaic growth defects and not to ion-beam damage. Mostly the defects lie along $\{111\}$ planes that is known [31] to be typical for twins. Due to the angle misalignment of the two crystals only a half of the image in Fig. 3(a) (right side) is in focus, while the left side is of less contrast. This can be further visualized with convergent-beam electron diffractions (CBED) patterns acquired from the left and right side of the junction as displayed in Figs. 3(c) and 3(d). The right crystal is placed at exact zone axis ($B = [110]$), the left crystal being slightly misoriented. The three misorientation angles are defined in Fig. 3(e): the angles α and γ denote out-of-plane misorientations due to rotation of the plates around the $[1\bar{1}0]$ axis and around the $[110]$ axis, respectively, while the rotation around the $[001]$ axis results in the in-plane misorientation angle β . We find the values $\alpha = 2.2^\circ$, $\beta = 0.7^\circ$, and $\gamma = 2.0^\circ$, which indicate the junction to be a low-angle grain boundary.

As the placement of the two seeds in proximity on the substrate holder before the growth process is performed manually, without an objective control, and because the real orientations of the polished facets of the seeds might deviate from the main crystallographic orientations, the nonzero misalignment angles seem to be inevitable and could be expected. Recently, Matsushita *et al.* [42] used electron backscatter diffraction (EBSD) technique to measure misalignment angles for a mosaic crystal composed of four plates prepared with “clone” seeds and liftoff [43]. They determined smaller misalignments $\alpha \approx 0.5^\circ$, $\beta = 0.5^\circ$, and $\gamma = 0.2^\circ$ presumably due to the better oriented individual clone seeds. The better alignment may result in a suppression of defect generation on the interface.

The densely arranged defects occupy the layer of approximately $1 \mu\text{m}$ thick on each side of the junction. The number of defects N reduces with distance (X) from the junction approximately following a Gaussian profile, with FWHM of approximately equal to $2.0 \mu\text{m}$ as shown in Fig. 3(f) [the defect profile $N(X)$ is plotted by counting the number of crossing points of linear defects with a vertical line at the distance X on the TEM image]. Interestingly, the junction line in the vertical plane is not perfectly straight but wavy, this reflecting nonplanar side walls of the growing blocks meeting at the interface. A local temporal variation in lateral growth rate of each block affected by surface features, such as, for example, steps, could be one of the reason for the observed nonideal junction geometry. On a larger scale the junction plane remains almost vertical, however, we do not exclude that at different growth parameters the interaction of two blocks could be more

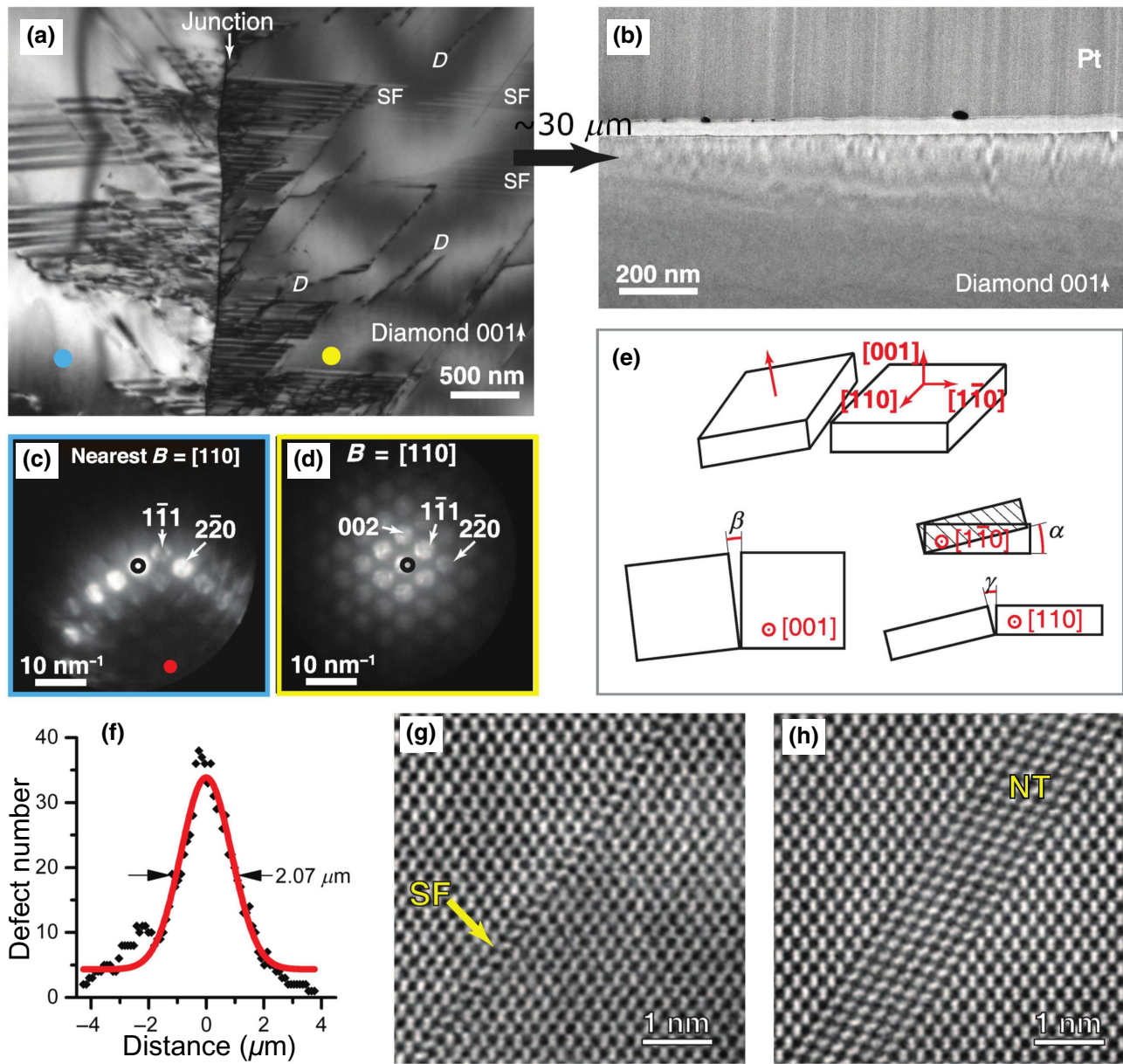


FIG. 3. (a) Low magnification bright-field (BF) TEM image of junction area. Stacking faults (SFs) and dislocations (D) are marked around the junction. Blue and yellow dots correspond to locations where CBED analysis is performed. (b) BF TEM image of a diamond crystal slice extracted $30 \mu\text{m}$ away from the junction, where no defects are seen. (c),(d) CBED patterns taken to the left and right of the junction, respectively, in its proximity [see (a)]. Black ring marks direct beam position. Red dot points to approximate position of zone axis $B = [110]$. (e) Schematics of two diamond crystals layout with the main crystallographic directions and misalignment angles α , β , γ . Open circles indicate direction normal to the drawing plane. (f) Distribution of density of defects $N(X)$ across the line normal to the junction between two blocks. The solid line is Gaussian fit with width (FWHM) of $2.07 \mu\text{m}$ centered on the junction. (g),(h) High-resolution HAADF STEM images of SF and nanotwin (NT) spreading from junction, respectively.

asymmetric, resulting in an inclined junction and dominating one of the blocks even if vertical growth rates are similar.

The STEM images with atomic resolution obtained with a high-angle annular dark-field detector (HAADF) reveal details of the structure of the most frequent defects in the junction zone, which are stacking faults SF, twins NT,

and combined defects, such as SF+NT, or multiple twins NT+NT. Examples of filtered HAADF STEM images of a stacking fault and single twin are given in Figs. 3(g) and 3(h). As mentioned earlier SF and NT lie along $\{111\}$ planes. Macroscopically the length of the defected zone along the large face of the bicrystal amounts to only approximately 0.04% of the total sample length of 5.4

mm, however it can induce a stress field spreading over distances of tens or even hundreds of micrometers from the junction [28,42]. This fact is helpful for thermal transport analysis as phonon scattering occurs both on defects and strained region. The defected zone around the junction in the mosaic diamond resembles the defects' distribution near GB in polycrystalline diamond films according to Steeds *et al.* [31], who observed with TEM a layer of the order of $1\ \mu\text{m}$ thick along GB enriched with defects, mostly microtwins.

B. Plasma etching of defects

It is known that the defects in diamond, specifically dislocations, exhibit area-selective enhanced etch rate in H_2 or $\text{H}_2\text{-O}_2$ microwave plasma, that is often used to detect and quantify those defects [44,45]. To visualize the defect-rich zone around the junction we expose the mosaic sample to $\text{H}_2 + \text{O}_2$ MW plasma for 15 min under the following parameters: pressure 70 Torr, MW power 3.0 kW, temperature $1000\ ^\circ\text{C}$, gas flow rate of 294 sccm for H_2 , and 6 sccm (2%) for O_2 .

Numerous square isolated etch pits with typical side length of approximately $200 - 400\ \text{nm}$, and clusters consisting of a few pits, corresponding to the surface and subsurface defects, presumably dislocations, could be seen on the optical microscope image (Fig. 4). The pits are uniformly distributed over the sample surface with density of the order of approximately $10^5\ \text{cm}^{-2}$ as revealed by surface imaging on a larger area (not shown here). In contrast, a groove of approximately $1\ \mu\text{m}$ wide is formed along the junction as a result of high defect concentration and enhanced etching of defective material around the junction. The groove has the depth of $0.45\ \mu\text{m}$ as illustrated on optical profilometer scan [Figs. 4(b) and 4(c)]. The groove width is in agreement with the width of defected zone around the junction as revealed by TEM analysis [see Fig. 3(b)].

C. Raman spectroscopy

To access the dimensions of the defected and stressed zone adjacent to the junction a mapping of diamond Raman peak position ν_R and peak width $\Delta\nu$ (FWHM) is performed in the vicinity of the junction (before plasma etching of the sample). Figure 5 (inset) compares the diamond Raman peak taken on a SCD block $150\ \mu\text{m}$ away from the junction, with that measured directly on the junction. The former spectrum reveals a narrow symmetric line with width $\Delta\nu$ of $2.5\ \text{cm}^{-1}$, while it notably broadens to $\Delta\nu \approx 4.4\ \text{cm}^{-1}$ on the junction, manifesting the presence of defects and/or nonuniform stress within the junction zone. The asymmetric peak on the junction can be deconvoluted to two more narrow peaks (not shown here) centered at $1333.4\ \text{cm}^{-1}$ and $1331.4\ \text{cm}^{-1}$, so the entire peak can be assigned to superposition of the response from slightly compressed and stretched domains, respectively. No features of amorphous carbon in the spectra are observed.

Figure 5 demonstrates how the Raman peak position and peak width vary when the laser-beam probe moves from one SCD block to another, crossing the junction in the middle. The distance X in the profiles $\nu_R(X)$ and $\Delta\nu(X)$ is counted from the junction line, from $-200\ \mu\text{m}$ to $+200\ \mu\text{m}$. The Raman peak width $\Delta\nu$ (bottom line in Fig. 5) is essentially broadened in a region of about $20\ \mu\text{m}$ wide around the junction, while the smaller peak width of approximately equal to $2.5\ \text{cm}^{-1}$, characteristic for high-quality diamond, is measured at distances $X > 15\ \mu\text{m}$ from the junction. This Raman peak broadening is caused by defects and spatially nonuniform defect-induced stress. The variation of strain within the micronscale-probed volume results in superposition of shifted Raman peaks from different locations within that volume, and thus, in the increase of the peak width. Therefore, the measured peak width allows a qualitative assessment of defect density in the crystal.

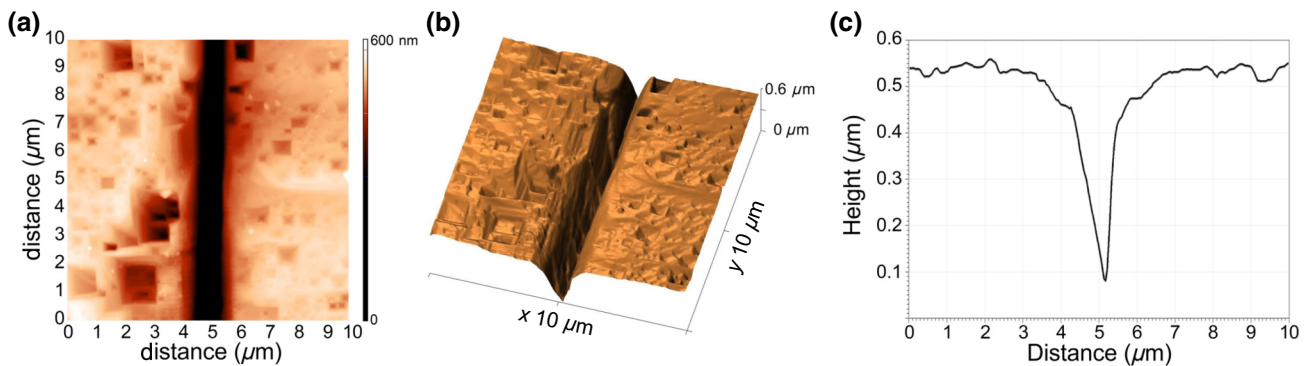


FIG. 4. Optical profilometry of a surface area $10 \times 10\ \mu\text{m}^2$ near the junction between two blocks of the mosaics after etching in $\text{H}_2\text{-O}_2$ microwave plasma. (a) Optical microscope image. Note a groove formed along the junction owing to preferential etching of the defected zone. (b) Three-dimensional (3D) surface profile across the groove. (c) Linear cross-section profile of the groove.

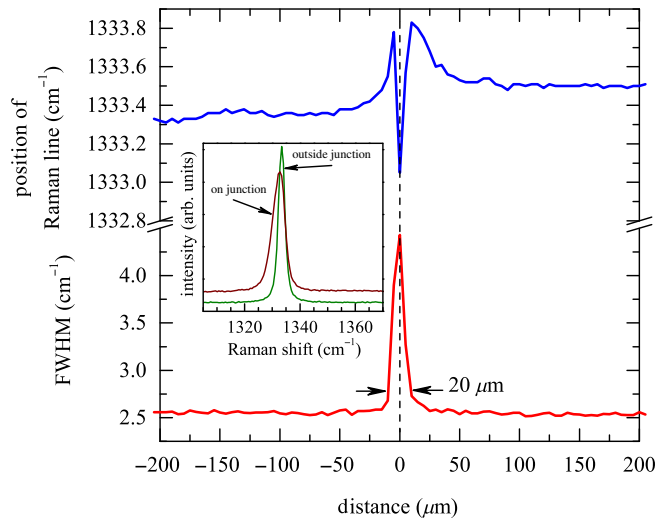


FIG. 5. Profiles of diamond Raman peak position $\nu_R(X)$ (top blue line) and the peak width (FWHM) $\Delta\nu(X)$ (bottom red line) on (100) face of the mosaic crystal along a path crossing the junction. The profile starts at one SCD block and ends on the adjacent block. The distance X is counted from the junction position ($X = 0$) marked by dashed vertical line. Inset: Raman spectra taken far from the junction ($X = +150 \mu\text{m}$, black line) and directly on the junction (brown line). Note the broadening of the peak on the junction. No normalization of the spectra is performed.

The deviation of the peak position ν_R from the normal value $\nu_{R0} = 1332.5 \text{ cm}^{-1}$ for unstressed diamond (for the spectrometer calibration we assign this value to the Raman peak for a high-quality type-IIa reference sample of natural diamond being in our disposal), is caused by a stress, the positive shift $\nu_R - \nu_{R0} > 0$ corresponding to compressive stress, while the opposite sign refers to a tensile stress. The variation of the Raman peak position $\nu_R(X)$ along the distance X shows (Fig. 5, top profile) almost symmetric but a more complex picture: the peak shifts to higher frequencies up to 1333.8 cm^{-1} on both sides of the junction, gradually decreasing within approximately $25 \mu\text{m}$ distance from the junction to a stable position at 1333.3 cm^{-1} outside this stressed (defected) zone. Closer to the junction, within approximately $10 \mu\text{m}$ wide zone around it, the peak position goes down to 1333.0 cm^{-1} , indicating a significant stress relaxation in proximity to the junction. It follows that the strain field extends from the junction to distances an order of magnitude larger compared to the width of defected zone as evaluated with TEM and plasma etching pattern. The maximum compressive stress $\sigma \approx 0.5 \text{ GPa}$ is estimated from the Raman peak position shift $\nu_R - \nu_{R0} \approx 1.1 \text{ cm}^{-1}$ using the relationship $\sigma = 0.38(\nu_R - \nu_{R0}) \text{ GPa/cm}^{-1}$ for hydrostatic stress [46]. In the model of biaxial stress within (100) plane, directed perpendicularly to the junction line, the relation $\sigma = 0.61(\nu_R - \nu_{R0}) \text{ GPa/cm}^{-1}$ (Ref. [47]) gives somewhat

larger value $\sigma \approx 0.8 \text{ GPa}$. Note, that the interior regions, distant from the junction, are under a low, uniform compressive stress as follows from the baseline Raman peak position at approximately equal to 1333.3 cm^{-1} .

D. Thermal conductivity

The temperature dependencies of thermal conductivity of the mosaic sample as measured within one single-crystal block (κ_{11}) and across the junction (κ_{12}), are displayed for the temperature range of 6–410 K in a log-log scale in Fig. 6, the inset shows the data in linear scale at high temperatures $T > 290 \text{ K}$ (the error bars represent the total errors, including systematic and random, of measurements). The $\kappa_{11}(T)$ exhibits an increase with T decrease down to $T_{\text{max}} = 77 \text{ K}$, where a maximum $\kappa_{\text{max}} = 183 \pm 4 \text{ W cm}^{-1} \text{ K}^{-1}$ is reached, and then it decreases towards low temperatures, to approximately equal to $6 \text{ W cm}^{-1} \text{ K}^{-1}$ at 6 K. A very high conductivity of value $24.0 \pm 0.5 \text{ W cm}^{-1} \text{ K}^{-1}$ is determined for the single block at room temperature (298.15 K). This can be compared with literature data on conductivity of most high-quality single-crystal CVD diamonds: $22.0 \text{ W cm}^{-1} \text{ K}^{-1}$ [2], $23.0 \pm 3.3 \text{ W cm}^{-1} \text{ K}^{-1}$ [16], $25.0 \pm 2.5 \text{ W cm}^{-1} \text{ K}^{-1}$ [48], and $\kappa \approx 20 \text{ W cm}^{-1} \text{ K}^{-1}$ for “white” polycrystalline CVD diamond [16]. The maximum conductivity κ_{max} for the SCD block is one of the highest ever reported, but still lower compared to that measured for most pure CVD diamonds ($278 \text{ W cm}^{-1} \text{ K}^{-1}$ at 62 K) [19] because of

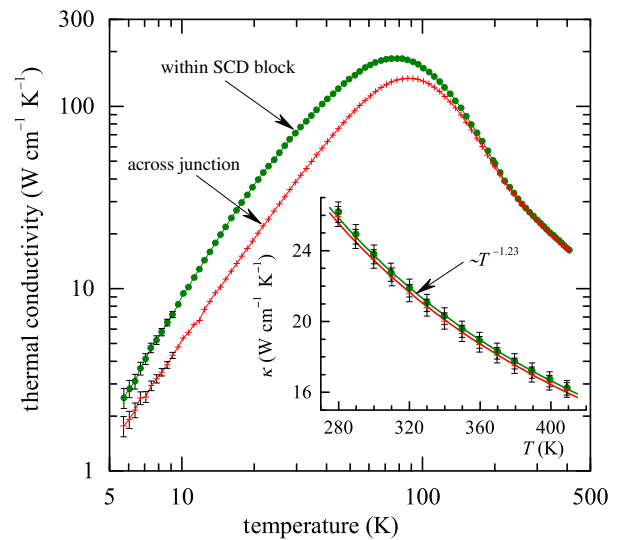


FIG. 6. Temperature dependence of thermal conductivity $\kappa(T)$ of the mosaics as measured within one crystal block (κ_{11} , circles) and across the junction (κ_{12} , crosses) in double logarithmic scale (for thermocouple positions see Fig. 2). The error bars are larger than the symbol size at temperatures below 9 K. Inset: the conductivity versus temperature in linear scale at high temperatures. The lines are fits $\kappa(T) = \kappa(298 \text{ K}) \times (T/298)^{-n}$.

significant nitrogen impurity present in the mosaic sample. The conductivities $\kappa_{11}(T)$ and $\kappa_{12}(T)$ are rather close to each other at high temperatures, but become diverge at low T (< 150 K), the conductivity across the junction significantly reducing, the ratio $\kappa_{11}(T)/\kappa_{12}(T)$ increasing to 1.32 at the conductivity maximum (77 K) and to approximately equal to 1.73 at 10 K. This clearly indicates the presence of a thermal barrier resistance at the interface between two single-crystal blocks of the mosaics, which gets more pronounced with temperature decrease.

The $\kappa(T)$ behavior at elevated temperatures 290–410 K is shown in more detail in the inset in Fig. 6. Both $\kappa_{11}(T)$ and $\kappa_{12}(T)$ decrease with temperature due to enhancing contribution of the anharmonic phonon-phonon scattering [12,13,49]. The curves $\kappa_{11}(T)$ and $\kappa_{12}(T)$ go nearly parallel, with the conductivity across the junction being systematically approximately equal to 2% lower than that for the SCD block. Particularly, the presence of the junction results in diminishing of conductivity from 24.0 ± 0.5 to 23.7 ± 0.5 $\text{W cm}^{-1} \text{K}^{-1}$ at 298 K. The observed (just small) effect of the junction on conductivity at room temperature is in agreement with results of Cheng *et al.* [50] who found only a minor variation (approximately 8%) in local conductivity near GB at room temperature for high-quality undoped thick PCD.

The $\kappa(T)$ curves above 290 K (Fig. 6, inset) can be approximated with a power law $\kappa(T) = \kappa(298 \text{ K}) \times (T/298 \text{ K})^{-n}$ known to hold above room temperature at least to 460 K [14,51]. We found the exponent

$n = 1.23 \pm 0.01$ to give a very good fit for the both curves. The values of $n = 1.26$ – 1.36 are typical for highest quality natural and HPHT diamonds of IIa type [14,51], while for the SCD with high nitrogen impurity content or low-grade polycrystalline CVD diamond with $\kappa(298 \text{ K}) = 6 - 8$ $\text{W cm}^{-1} \text{K}^{-1}$, the exponent n reduces to the values as low as 0.2–0.6. Thus we confirm, now for the single-crystal CVD diamond, the previously deduced trend for exponent n versus diamond quality.

The measurements of $\kappa_{11}(T)$ performed at different positions of the thermopile on the single-crystal block gave the same value of thermal conductivity within the experimental error in the whole temperature range under investigation. Also we check in the measurement of $\kappa(T)$ on the adjacent single block that it had the similar high quality as the counterpart block, with almost identical ($< 1\%$ difference) curve $\kappa(T)$. Similar repeated measurements are performed for $\kappa_{12}(T)$ by shifting the line between points 3 and 4 along the junction (Fig. 2), and, again, we reveal high reproducibility for the κ_{12} value. Therefore, the divergence for $\kappa_{11}(T)$ and $\kappa_{12}(T)$, seen in Fig. 6 is caused mostly by the presence of thermal-barrier resistance induced by the interblock junction.

E. Thermal boundary resistance

We estimate the junction thermal barrier resistance $R_j(T)$ from the measured difference of κ_{11} and κ_{12} . Assuming the two crystal blocks to have identical quality and

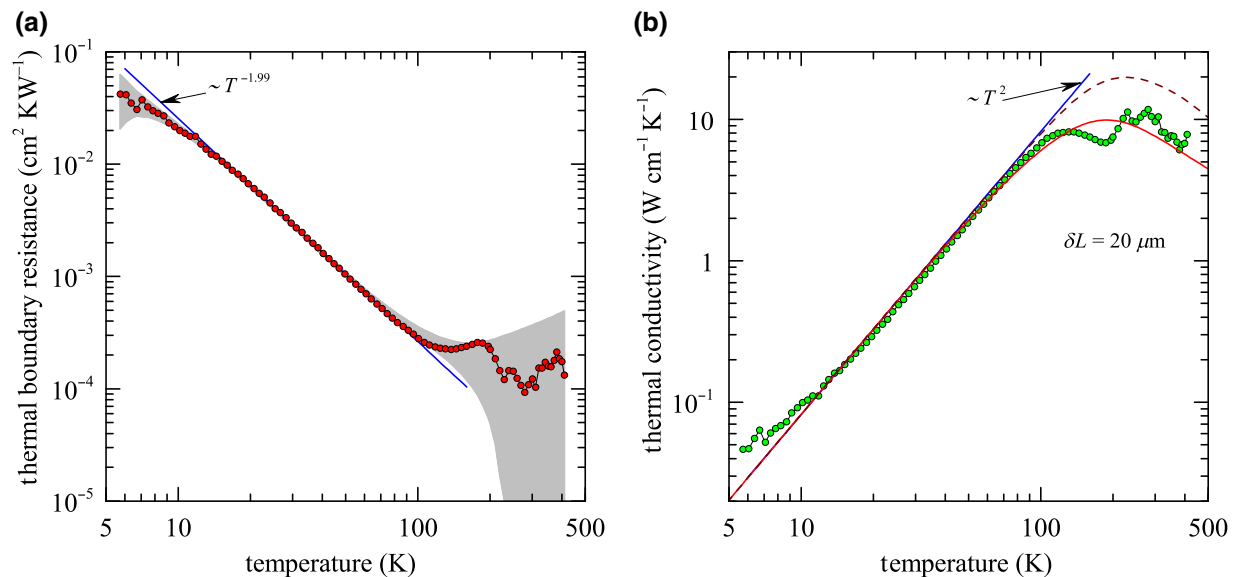


FIG. 7. (a) Thermal boundary resistance R_j between two single-crystal blocks as a junction of temperature. Circles are experimental data; the solid line is the best fit of power function to these data. The gray shaded area corresponds to the uncertainty in smoothed experimental data. (b) The effective local thermal conductivity $\kappa_j(T)$ of the defected layer of $20 \mu\text{m}$ width around the junction. Circles are experimental data. Solid red line represents the calculated $\kappa_j(T)$, the best fit of the model to experimental data. The straight solid line shows $\kappa_j(T) \sim T^2$ dependence. The dashed line shows $\kappa_j(T)$ for the case of point defect-free crystal except of the ^{13}C isotopes ($A_{\text{PD}} = A_{\text{iso}}$).

conductivity of κ_{11} , the R_j value is found from equation $L/\kappa_{12} = L/\kappa_{11} + R_j$, where L is the distance between the thermocouple junctions. The temperature dependence $R_j(T)$ is displayed in Fig. 7(a). The conductivities κ_{11} and κ_{12} are measured in different areas of the same sample. The sample and its heater are not disassembled between these experiments, and only the battery of thermocouples moved over the sample surface. Due to these circumstances, some systematic errors, for example, errors due to the geometric factor, heat losses, are the same for the measured κ_{11} and κ_{12} , and they are excluded (in the first approximation) when calculating the total error of the thermal resistance of the junction. Systematic error reduced from 2% to 1%. In Fig. 7(a), the gray shaded area corresponds to the uncertainty in smoothed experimental data. The upper and lower boundaries of this area are $\bar{R}_j + \delta R_j$ and $\bar{R}_j - \delta R_j$, respectively, with \bar{R}_j being the smooth approximation of the “experimental” dependence. The absolute error δR_j is defined as $\delta R_j = L(\delta\kappa/\kappa) (\kappa_{11}^{-2} + \kappa_{12}^{-2})^{1/2}$, where $\delta\kappa/\kappa$ is the relative error of the measured value of thermal conductivity (we assume that this error is approximately the same for both κ_{11} and κ_{12}).

From 14 to 83 K the experimental data $R_j(T)$ nicely follow the dependence $R_j(T) \sim T^{-1.99}$ as shown by a solid line in log-log scale in Fig. 7(a). The TBR is as high as approximately equal to $4 \times 10^{-2} \text{ cm}^2 \text{ K W}^{-1}$ at 6 K, but decreases to relatively low value approximately equal to $2 \times 10^{-4} \text{ cm}^2 \text{ K W}^{-1}$ at $T > 100$ K. These low TBR values are within the measurement uncertainty at high temperatures above $T \approx 150$ K. We note that the determined TBR value for the mosaic diamond at room temperature is comparable to TBR of $(1.7 - 3.2) \times 10^{-4} \text{ cm}^2 \text{ K W}^{-1}$ for interface GaN-diamond with 20–30-nm-thick SiN interlayer reported by Cho *et al.* [52] and grain-grain thermal resistance of $(6 - 600) \times 10^{-4} \text{ cm}^2 \text{ K W}^{-1}$ (Ref. [53]), or $(0.3 - 1.8) \times 10^{-5} \text{ cm}^2 \text{ K W}^{-1}$ (Ref. [15]) on grain boundaries in thin (1 μm) nanocrystalline diamond films.

The thermal boundary resistance of the interface between single-crystal blocks within the acoustic mismatch model and the Debye approximation of the phonon spectrum can be evaluated by using the following expression (Ref. [54], page 620):

$$R_j = \left(1.02 \times 10^{10} \left[\sum_i c_i^{-2} \right] \right)^{-1} T^{-3}, \quad (1)$$

where c_i are the sound velocities, one longitudinal (L) and two transverse (T), in cm/s; R_j in $\text{cm}^2 \text{ K W}^{-1}$. Taking $c_L = 17.5 \times 10^5 \text{ cm/s}$ and $c_T = 12.8 \times 10^5 \text{ cm/s}$ (see, e.g. Ref. [54], page 620), we arrive at $R_j \approx 2.4 \times 10^{-6} \text{ cm}^2 \text{ K W}^{-1}$ at 300 K. The diffuse mismatch model yields twofold higher value in our case (Ref. [54], page 623). The value of TBR at 300 K we obtain from the experiment, is more than 1–2 orders of magnitude higher than

the theoretical estimate. The observed temperature dependence of TBR is substantially weaker than the T^3 at low temperatures expected within the theoretical models [54]. This suggests the measured TBR to be in fact an effective thermal boundary resistance caused in a great extent by phonon scattering off imperfections next to the interface between crystallites, and only little by the interface itself. This picture of the thermal transport is similar to that proposed in Refs. [15,36]. The total width ΔL of the highly defected zone summed on both sides of the crystal junction, is approximately 2–4 μm as deduced from TEM analysis [Fig. 3(b)], and approximately equal to 20 μm as follows from Raman spectrum broadening (Fig. 5). Interestingly, the latter value is close to the doubled distance of 10 μm from the GB for which a reduction in thermal conductivity within an individual grain in a PCD wafer was observed by Sood *et al.* [39]. Assuming the local thermal conductivity in that defective layer to be spatially constant, and neglecting the contribution of the interface boundary resistance, we obtain the average thermal conductivity κ_j of the adjacent defective layer according to $R_j = \Delta L/\kappa_j$, with $\Delta L \approx 20 \mu\text{m}$. The plot $\kappa_j(T)$ displayed in Fig. 7(b) is actually the scaled reversed plot of $R_j(T)$, it reveals a significantly reduced conductivity near the junction, of approximately equal to 6–10 $\text{W cm}^{-1} \text{ K}^{-1}$ at temperatures above 100 K. Such low values are comparable with the conductivity of low-grade polycrystalline diamond films [14,55,56], or thin (a few microns) microcrystalline diamond films [57], but much lower than the measured conductivities κ_{11} and κ_{12} for the mosaic. The effective junction conductivity $\kappa_j(T)$ varies as T^2 at $T < 100$ K as shown in Fig. 7(b), indicating a strong effect of lattice imperfections on thermal transport within the layer around the junction. Point defects mostly contribute to thermal resistance at higher temperatures (> 100 K), while, additionally, phonon-phonon scattering enhances roughly above room temperature. Klemens [58] and Caruthers [59,60] shown theoretically that under the dominance of the phonon scattering from dislocations over all other processes the $\kappa(T)$ should have a T^2 dependence. We approximate $\kappa_j(T)$ using the phenomenological model proposed in Ref. [19], based on the full Callaway theory [61] with the parameters describing the intrinsic anharmonic three-phonon processes determined from the best fit of the model to experimental data for high-purity single-crystal diamonds [19]. Here we add to the model the phonon scattering from static strain field surrounding dislocations [60]. The rate of this scattering from an array of randomly oriented independent edge and screw dislocations is [60]

$$\tau^{-1} \approx \rho_d b^2 \gamma^2 \omega = A_d x T, \quad (2)$$

where ρ_d is the density of dislocations per unit area, b is the Burgers vector of the dislocation, γ is the Grüneisen parameter, ω is the phonon frequency, and $x = \hbar\omega/k_B T$,

where \hbar is Planck constant and k_B is Boltzmann constant. The semiquantitative nature of this expression has been confirmed recently by Li *et al.* [62], Sun *et al.* [63], and Li *et al.* [64]. In our calculations, the rates of point defect and dislocation scatterings are adjustable parameters, and the phonon free path l_b in the boundary scattering is taken constant. The $l_b = 5.8$ nm is determined from the fitting of the model to the experimental data $\kappa(T)$ for the single-crystal block, in which the dislocation scattering is negligible. With optimized parameter $A_d = 1.0 \times 10^7 \text{ s}^{-1}\text{K}^{-1}$ the model yields very good approximation for the experimental $\kappa_j(T)$ down to $T = 10$ K as the Fig. 7(b) evidences. Taking $\gamma \approx 1.1$ (Ref. [65]) and $b \approx \sqrt{2}/3a$, $a = 3.567 \text{ \AA}$ is the lattice constant, we find for the dislocation density $\rho_d \approx 2.2 \times 10^{11} \text{ cm}^{-2}$. Since Carruthers' theory underestimates the rate of dislocation scattering by 4–6 times [60,63], a more realistic estimate of the dislocation density would be $\rho_d \leq 5 \times 10^{10} \text{ cm}^{-2}$, which is in qualitative agreement with ρ_d in polycrystalline CVD diamonds (see, e.g., Ref. [13]) and within junction zone of mosaic crystals as reported by Ohmagari *et al.* [29].

For the phonon-scattering rate by point defects τ_{PD}^{-1} in our calculations we use the standard expression of the Rayleigh type $\tau_{\text{PD}}^{-1} = A_{\text{PD}}x^4T^4$. The best fitting is obtained with $A_{\text{PD}} = 6.7 \times 10^{-2} \text{ s}^{-1}\text{K}^{-4}$. This value exceeds by 16 times the value for a perfect crystal of diamond with natural isotopic composition [19]. The very high value of thermal conductivity for single-crystal block near the room temperature indicates very weak phonon scattering by point defects other than the isotope ^{13}C atoms. Optical spectroscopy has not detected defect centers in substantial concentrations except the nitrogen with content below 3 ppm. Therefore, highly likely the vacancies and their complexes are those point defects in the 20- μm -wide layer near the junction that reduce much thermal conductivity here. Using the expression for the phonon scattering by single vacancies after Ratsifaritana and Klemens [66] with a correction proposed recently by Katcho *et al.* [67] we estimate the concentration of vacancies within the 20- μm layer to be about 30 ppm ($5.5 \times 10^{18} \text{ cm}^{-3}$).

Our Raman studies find a compressive stresses with a maximum value of approximately equal to 0.5 GPa around the junction, that hypothetically could alter the magnitude of $\kappa(T)$. To our knowledge, there are no experimental data on thermal conductivity of diamond as a function of applied pressure. *Ab initio* calculations [68] show that hydrostatic pressure increases the thermal conductivity of diamond at temperatures above 80 K, the conductivity increases slightly, by 0.5% at pressure of 0.5 GPa at 300 K. We find the opposite result: suppressed conductivity near the junction. Obviously, lattice defects near the junction decrease the thermal conductivity much more strongly than compressive stresses increase it.

Molecular dynamics (MD) simulation of heat transport in NCD films assuming the thickness of GB of a few

atomic distances (with no defects outside of the GB) [69] results in a TBR lower limit of $10^{-7} - 10^{-6} \text{ cm}^2 \text{ K W}^{-1}$ at room temperature, 2–3 orders of magnitude lower with respect to our TBR data. However, one should bear in mind that the TBR measured here is an effective value, with contributions of the junction itself and the defect zone field around it, which could not be discriminated in the present experiment. The TBR of the interface itself, of atomic scale thickness, could be much less than $10^{-4} \text{ cm}^2 \text{ K W}^{-1}$, that is closer to the values expected from the MD simulation. On the other hand, it would be possible to further reduce the effective TBR for mosaic crystals provided a more regular interface between block would be organized, the later requires a better control for orientation of the faces of the seeds, and their alignment on substrate holder in the reactor.

IV. CONCLUSIONS

In summary, using a steady-state longitudinal heat-flow method we precisely measure the *in-plane* thermal conductivity $\kappa(T)$ of a diamond mosaic crystal in the broad temperature range of 6–410 K. The single-crystal blocks of the mosaic grown by microwave plasma CVD revealed conductivity of $24.0 \pm 0.5 \text{ W cm}^{-1} \text{ K}^{-1}$, one of the highest ever reported for diamond at room temperature. However, when the heat flux crosses the junction between two adjacent blocks, the conductivity reduces by a few percent, due to thermal resistance R_j of the junction. Being low at room temperature, $R_j(298) \approx 2 \times 10^{-4} \text{ cm}^2 \text{ K W}^{-1}$, the TBR strongly increases below 100 K. Towards low temperatures the impact of the junction TBR becomes significant, resulting in reduction of $\kappa(T)$ by a factor of 1.75 at 10 K compared to that for single-crystal block.

Combining TEM analysis, Raman spectroscopy, and plasma-surface etching we ascertain distribution of defects and stress in the vicinity of the junction, which contribute to the observed thermal boundary resistance. The complex structure of the junction region consists of three zones with different length scales: (i) atomic scale interface between the crystals; (ii) an approximately 1- μm -thick layer in proximity to the interface, highly enriched with defects such as dislocations, twins, and stacking faults; and (iii) an approximately 10- μm -thick layer of enhanced stressed. The interface itself leads to only negligible TBR according to our modeling, rather the actual local thermal resistance near the block's junction is caused by the defected and stressed zone around the junction. The phonon scattering by dislocations dominates at temperatures below 100 K and results in temperature dependence of the junction thermal resistance $R_j(T) \sim T^2$ in the low-temperature domain. At $100 < T < 410$ K the point-defect scattering and intrinsic phonon-phonon scattering processes determine the local thermal resistance. We show that the diamond mosaics preserve excellent thermal properties of

the constituent single-crystal blocks at room and higher temperatures, and can be used as heat spreaders as effectively as the single crystals.

ACKNOWLEDGMENTS

The work is supported by the Russian Foundation for Basic Research (Grant No. 19-52-53019), National Natural Science Foundation of China (Grant No. 52072087), 1000 Talents program, and National Science Fund for Distinguished Young Scholars (Grant No. 51625201). A.V.I. and I.A.K. acknowledge the support from NRC “Kurchatov Institute” and the Russian Foundation for Basic Research (Grant No. 19-07-00229) in the part of work related to thermal conductivity and TEM measurements.

-
- [1] S. Shikata, Single crystal diamond wafers for high power electronics, *Diamond Relat. Mater.* **65**, 168 (2016).
- [2] R. S. Balmer, J. R. Brandon, S. L. Clewes, H. K. Dhillon, J. M. Dodson, I. Friel, P. N. Inglis, T. D. Madgwick, M. L. Markham, T. P. Mollart, N. Perkins, G. A. Scarsbrook, D. J. Twitchen, A. J. Whitehead, J. J. Wilman, and S. M. Woollard, Chemical vapour deposition synthetic diamond: Materials, technology and applications, *J. Phys. Condens. Matter* **21**, 364221 (2009).
- [3] A. E. Helou, P. Komarov, M. J. Tadjer, T. J. Anderson, D. A. Francis, T. Feygelson, B. B. Pate, K. D. Hobart, and P. E. Raad, High-resolution thermoreflectance imaging investigation of self-heating in AlGaIn/GaN HEMTs on Si, SiC, and diamond substrates, *IEEE Trans. Electron Devices* **67**, 5415 (2020).
- [4] R. S. Sussmann, ed., *CVD Diamond for Electronic Devices and Sensors* (John Wiley & Sons, Ltd, Chichester, UK, 2009).
- [5] D. E. Field, J. A. Cuenca, M. Smith, S. M. Fairclough, F. C.-P. Massabuau, J. W. Pomeroy, O. Williams, R. A. Oliver, I. Thayne, and M. Kuball, Crystalline interlayers for reducing the effective thermal boundary resistance in GaN-on-diamond, *ACS Appl. Mater. Interfaces* **12**, 54138 (2020).
- [6] M. J. Tadjer, T. J. Anderson, M. G. Ancona, P. E. Raad, P. Komarov, T. Bai, J. C. Gallagher, A. D. Koehler, M. S. Goorsky, D. A. Francis, K. D. Hobart, and F. J. Kub, GaN-on-diamond HEMT technology with TAVG = 176°C at PDC, max = 56 W/mm measured by transient thermoreflectance imaging, *IEEE Electron Device Lett.* **40**, 881 (2019).
- [7] J. Yu, G. Liu, A. V. Sumant, V. Goyal, and A. A. Balandin, Graphene-on-diamond devices with increased current-carrying capacity: Carbon sp²-on-sp³ technology, *Nano Lett.* **12**, 1603 (2012).
- [8] J.-H. Wolter, R. Balmer, S. Ricaud, M. Antier, C. Simon-Boisson, T. Graf, and M. A. Ahmed, Ti:sapphire thin-disk laser symmetrically cooled by curved single crystal diamond heat spreaders, *Laser Phys. Lett.* **17**, 015802 (2019).
- [9] G. Gantenbein, A. Samartsev, G. Aiello, G. Dammertz, J. Jelonnek, M. Losert, A. Schlaich, T. A. Scherer, D. Strauss, M. Thumm, and D. Wagner, First operation of a step-frequency tunable 1-MW gyrotron with a diamond Brewster angle output window, *IEEE Trans. Electron Devices* **61**, 1806 (2014).
- [10] E. Anoikin, A. Muhr, A. Bennett, D. Twitchen, and H. de Wit, in *Proc. SPIE, Components and Packaging for Laser Systems* (SPIE - International Society for Optics and Photonics, 2015), Vol. 9346, p. 93460T.
- [11] R. B. Simon, J. Anaya, F. Faili, R. Balmer, G. T. Williams, D. J. Twitchen, and M. Kuball, Effect of grain size of polycrystalline diamond on its heat spreading properties, *Appl. Phys. Express* **9**, 061302 (2016).
- [12] A. V. Inyushkin, A. N. Taldenkov, V. G. Ral'chenko, V. I. Konov, A. V. Khomich, and R. A. Khmel'nitski, Thermal conductivity of polycrystalline CVD-diamond: Experiment and theory, *JETP* **107**, 462 (2008).
- [13] J. E. Graebner, M. E. Reiss, L. Seibles, T. M. Hartnett, R. P. Miller, and C. J. Robinson, Phonon scattering in chemical-vapor-deposited diamond, *Phys. Rev. B* **50**, 3702 (1994).
- [14] A. V. Sukhadolau, E. V. Ivakin, V. G. Ralchenko, A. V. Khomich, A. V. Vlasov, and A. F. Popovich, Thermal conductivity of CVD diamond at elevated temperatures, *Diamond Relat. Mater.* **14**, 589 (2005).
- [15] J. Anaya, T. Bai, Y. Wang, C. Li, M. Goorsky, T. L. Bougher, L. Yates, Z. Cheng, S. Graham, K. D. Hobart, T. I. Feygelson, M. J. Tadjer, T. J. Anderson, B. B. Pate, and M. Kuball, Simultaneous determination of the lattice thermal conductivity and grain/grain thermal resistance in polycrystalline diamond, *Acta Mater.* **139**, 215 (2017).
- [16] A. P. Bolshakov, V. G. Ralchenko, V. Y. Yurov, A. F. Popovich, I. A. Antonova, A. A. Khomich, E. E. Ashkinazi, S. G. Ryzhkov, A. V. Vlasov, and A. V. Khomich, High-rate growth of single crystal diamond in microwave plasma in CH₄/H₂ and CH₄/H₂/Ar gas mixtures in presence of intensive soot formation, *Diamond Relat. Mater.* **62**, 49 (2016).
- [17] D. J. Twitchen, C. S. J. Pickles, S. E. Coe, R. S. Sussmann, and C. E. Hall, Thermal conductivity measurements on CVD diamond, *Diamond Relat. Mater.* **10**, 731 (2001).
- [18] Qinyu Kong, Alvarado Tarun, Chuan Ming Yap, Siwei Xiao, Kun Liang, Beng Kang Tay, and Devi Shanker Misra, Influence of optically active defects on thermal conductivity of polycrystalline diamond, *Eur. Phys. J. Appl. Phys.* **80**, 20102 (2017).
- [19] A. V. Inyushkin, A. N. Taldenkov, V. G. Ralchenko, A. P. Bolshakov, A. V. Koliadin, and A. N. Katrusha, Thermal conductivity of high purity synthetic single crystal diamonds, *Phys. Rev. B* **97**, 144305 (2018).
- [20] M. Schreck, J. Asmussen, S. Shikata, J.-C. Arnault, and N. Fujimori, Large-area high-quality single crystal diamond, *MRS Bull.* **39**, 504 (2014).
- [21] M. Schreck, S. Gsell, R. Brescia, and M. Fischer, Ion bombardment induced buried lateral growth: The key mechanism for the synthesis of single crystal diamond wafers, *Sci. Rep.* **7**, 44462 (2017).
- [22] H. Aida, S.-W. Kim, K. Ikejiri, Y. Kawamata, K. Koyama, H. Kodama, and A. Sawabe, Fabrication of free-standing heteroepitaxial diamond substrate via micropatterns and microneedles, *Appl. Phys. Express* **9**, 035504 (2016).

- [23] M. W. Geis, H. I. Smith, A. Argoitia, J. Angus, G.-H. M. Ma, J. T. Glass, J. Butler, C. J. Robinson, and R. Pryor, Large-area mosaic diamond films approaching single-crystal quality, *Appl. Phys. Lett.* **58**, 2485 (1991).
- [24] G. Janssen and L. J. Giling, “Mosaic” growth of diamond, *Diamond Relat. Mater.* **4**, 1025 (1995).
- [25] H. Yamada, A. Chayahara, Y. Mokuno, N. Tsubouchi, and S. Shikata, Uniform growth and repeatable fabrication of inch-sized wafers of a single-crystal diamond, *Diamond Relat. Mater.* **33**, 27 (2013).
- [26] H. Yamada, A. Chayahara, Y. Mokuno, Y. Kato, and S. Shikata, A 2-in. mosaic wafer made of a single-crystal diamond, *Appl. Phys. Lett.* **104**, 102110 (2014).
- [27] H. Yamada, A. Meier, F. Mazzocchi, S. Schreck, and T. Scherer, Dielectric properties of single crystalline diamond wafers with large area at microwave wavelengths, *Diamond Relat. Mater.* **58**, 1 (2015).
- [28] G. Shu, B. Dai, V. G. Ralchenko, A. A. Khomich, E. E. Ashkinazi, A. P. Bolshakov, S. N. Bokova-Sirosh, K. Liu, J. Zhao, J. Han, and J. Zhu, Epitaxial growth of mosaic diamond: Mapping of stress and defects in crystal junction with a confocal Raman spectroscopy, *J. Cryst. Growth* **463**, 19 (2017).
- [29] S. Ohmagari, H. Yamada, N. Tsubouchi, H. Umezawa, A. Chayahara, A. Seki, F. Kawaii, H. Saitoh, and Y. Mokuno, Schottky barrier diodes fabricated on diamond mosaic wafers: Dislocation reduction to mitigate the effect of coalescence boundaries, *Appl. Phys. Lett.* **114**, 082104 (2019).
- [30] X. Wang, P. Duan, Z. Cao, C. Liu, D. Wang, Y. Peng, X. Xu, and X. Hu, Surface morphology of the interface junction of CVD mosaic single-crystal diamond, *Materials* **13**, 91 (2020).
- [31] J. W. Steeds, A. Gilmore, K. M. Bussmann, J. E. Butler, and P. Koidl, On the nature of grain boundary defects in high quality CVD diamond films and their influence on physical properties, *Diamond Relat. Mater.* **8**, 996 (1999).
- [32] J. Hartmann, M. Costello, and M. Reichling, Influence of Thermal Barriers on Heat Flow in High Quality Chemical Vapor Deposited Diamond, *Phys. Rev. Lett.* **80**, 117 (1998).
- [33] W. L. Liu, M. Shamsa, I. Calizo, A. A. Balandin, V. Ralchenko, A. Popovich, and A. Saveliev, Thermal conduction in nanocrystalline diamond films: Effects of the grain boundary scattering and nitrogen doping, *Appl. Phys. Lett.* **89**, 171915 (2006).
- [34] M. A. Angadi, T. Watanabe, A. Bodapati, X. Xiao, O. Auciello, J. A. Carlisle, J. A. Eastman, P. Koblinski, P. K. Schelling, and S. R. Phillpot, Thermal transport and grain boundary conductance in ultrananocrystalline diamond thin films, *J. Appl. Phys.* **99**, 114301 (2006).
- [35] A. V. Inyushkin, A. N. Taldenkov, V. G. Ralchenko, I. I. Vlasov, V. I. Konov, A. V. Khomich, R. A. Khmel'nitskii, and A. S. Trushin, Thermal conductivity of polycrystalline CVD diamond: Effect of annealing induced transformations of defects and grain boundaries, *Phys. Status Solidi A* **205**, 2226 (2008).
- [36] J. Anaya, S. Rossi, M. Alomari, E. Kohn, L. Tóth, B. Pécz, K. D. Hobart, T. J. Anderson, T. I. Feygelson, B. B. Pate, and M. Kuball, Control of the in-plane thermal conductivity of ultra-thin nanocrystalline diamond films through the grain and grain boundary properties, *Acta Mater.* **103**, 141 (2016).
- [37] A. Sood, J. Cho, K. D. Hobart, T. I. Feygelson, B. B. Pate, M. Asheghi, D. G. Cahill, and K. E. Goodson, Anisotropic and inhomogeneous thermal conduction in suspended thin-film polycrystalline diamond, *J. Appl. Phys.* **119**, 175103 (2016).
- [38] Z. Cheng, T. Bougher, T. Bai, S. Y. Wang, C. Li, L. Yates, B. M. Foley, M. Goorsky, B. A. Cola, F. Faili, and S. Graham, Probing growth-induced anisotropic thermal transport in high-quality CVD diamond membranes by multifrequency and multiple-spot-size time-domain thermoreflectance, *ACS Appl. Mater. Interfaces* **10**, 4808 (2018).
- [39] A. Sood, R. Cheaito, T. Bai, H. Kwon, Y. Wang, C. Li, L. Yates, T. Bougher, S. Graham, M. Asheghi, M. S. Goorsky, and K. E. Goodson, Direct visualization of thermal conductivity suppression due to enhanced phonon scattering near individual grain boundaries, *Nano Lett.* **18**, 3466 (2018).
- [40] S. V. Nistor, M. Stefan, V. Ralchenko, A. Khomich, and D. Schoemaker, Nitrogen and hydrogen in thick diamond films grown by microwave plasma enhanced chemical vapor deposition at variable H₂ flow rates, *J. Appl. Phys.* **87**, 8741 (2000).
- [41] S. Rubanov, in *European Microscopy Congress 2016: Proceedings* (American Cancer Society, Wiley-VCH Verlag GmbH & Co. KGaA, 2016), p. 358.
- [42] A. Matsushita, N. Fujimori, Y. Tsuchida, N. Ohtani, D. Dojima, K. Koide, T. Kaneko, and S. Shikata, Evaluation of diamond mosaic wafer crystallinity by electron backscatter diffraction, *Diamond Relat. Mater.* **101**, 107558 (2020).
- [43] H. Yamada, A. Chayahara, Y. Mokuno, H. Umezawa, S. Shikata, and N. Fujimori, Fabrication of 1 inch mosaic crystal diamond wafers, *Appl. Phys. Express* **3**, 051301 (2010).
- [44] A. Tallaire, T. Ouisse, A. Lantreibecq, R. Cours, M. Legros, H. Bensalah, J. Barjon, V. Mille, O. Brinza, and J. Achard, Identification of dislocations in synthetic chemically vapor deposited diamond single crystals, *Cryst. Growth Des.* **16**, 2741 (2016).
- [45] V. Yurov, E. Bushuev, A. Bolshakov, E. Ashkinazi, I. Antonova, E. Zavedeev, A. Khomich, V. Voronov, and V. Ralchenko, Etching kinetics of (100) single crystal diamond surfaces in a hydrogen microwave plasma, studied with in situ low-coherence interferometry, *Phys. Status Solidi A* **214**, 1700177 (2017).
- [46] A. Tardieu, F. Cansell, and J. P. Petit, Pressure and temperature dependence of the first-order Raman mode of diamond, *J. Appl. Phys.* **68**, 3243 (1990).
- [47] J. W. Ager III and M. D. Drory, Quantitative measurement of residual biaxial stress by Raman spectroscopy in diamond grown on a Ti alloy by chemical vapor deposition, *Phys. Rev. B* **48**, 2601 (1993).
- [48] Y. Yamamoto, T. Imai, K. Tanabe, T. Tsuno, Y. Kumazawa, and N. Fujimori, The measurement of thermal properties of diamond, *Diamond Relat. Mater.* **6**, 1057 (1997).
- [49] D. T. Morelli, J. P. Heremans, and G. A. Slack, Estimation of the isotope effect on the lattice thermal conductivity of

- group IV and group III-V semiconductors, *Phys. Rev. B* **66**, 195304 (2002).
- [50] Z. Cheng, R. Cheaito, T. Bai, L. Yates, A. Sood, B. Foley, T. Bougher, F. Faili, M. Asheghi, K. Goodson, B. Cola, M. Goorsky, and S. Graham, in *International Heat Transfer Conference (IHTC-16)*, 2018, 10-15 August, Beijing, China (AIHTC, Beijing, 2018), p. 8694.
- [51] E. A. Burgemeister, Thermal conductivity of natural diamond between 320 and 450 K, *Physica B+C* **93**, 165 (1978).
- [52] J. Cho, D. Francis, D. H. Altman, M. Asheghi, and K. E. Goodson, Phonon conduction in GaN-diamond composite substrates, *J. Appl. Phys.* **121**, 055105 (2017).
- [53] M. Nazari, B. L. Hancock, J. Anderson, K. D. Hobart, T. I. Feygelson, M. J. Tadjer, B. B. Pate, T. J. Anderson, E. L. Piner, and M. W. Holtz, Optical characterization and thermal properties of CVD diamond films for integration with power electronics, *Solid-State Electron.* **136**, 12 (2017).
- [54] E. T. Swartz and R. O. Pohl, Thermal boundary resistance, *Rev. Mod. Phys.* **61**, 605 (1989).
- [55] S. D. Wolter, D.-A. Borca-Tasciuc, G. Chen, N. Govindaraju, R. Collazo, F. Okuzumi, J. T. Prater, and Z. Sitar, Thermal conductivity of epitaxially textured diamond films, *Diamond Relat. Mater.* **12**, 61 (2003).
- [56] A. F. Popovich, V. G. Ralchenko, V. K. Balla, A. K. Mallik, A. A. Khomich, A. P. Bolshakov, D. N. Sovyk, E. E. Ashkinazi, and V. Y. Yurov, Growth of 4" diameter polycrystalline diamond wafers with high thermal conductivity by 915 MHz microwave plasma chemical vapor deposition, *Plasma Sci. Technol.* **19**, 035503 (2017).
- [57] J. E. Graebner, V. G. Ralchenko, A. A. Smolin, E. D. Obratsova, K. G. Korotushenko, and V. I. Konov, Thermal conductivity of thin diamond films grown from d.c. discharge, *Diamond Relat. Mater.* **5**, 693 (1996).
- [58] P. G. Klemens, The scattering of low-frequency lattice waves by static imperfections, *Proc. Phys. Soc., London, Sec. A* **68**, 1113 (1955).
- [59] P. Carruthers, Scattering of phonons by elastic strain fields and the thermal resistance of dislocations, *Phys. Rev.* **114**, 995 (1959).
- [60] P. Carruthers, Theory of thermal conductivity of solids at low temperatures, *Rev. Mod. Phys.* **33**, 92 (1961).
- [61] J. Callaway, Model for lattice thermal conductivity at low temperatures, *Phys. Rev.* **113**, 1046 (1959).
- [62] M. Li, Z. Ding, Q. Meng, J. Zhou, Y. Zhu, H. Liu, M. S. Dresselhaus, and G. Chen, Nonperturbative quantum nature of the dislocation-phonon interaction, *Nano Lett.* **17**, 1587 (2017).
- [63] B. Sun, G. Haunschild, C. Polanco, J. Ju, L. Lindsay, G. Koblmüller, and Y. K. Koh, Dislocation-induced thermal transport anisotropy in single-crystal group-III nitride films, *Nat. Mater.* **18**, 136 (2019).
- [64] H. Li, R. Hanus, C. A. Polanco, A. Zeidler, G. Koblmüller, Y. K. Koh, and L. Lindsay, GaN thermal transport limited by the interplay of dislocations and size effects, *Phys. Rev. B* **102**, 014313 (2020).
- [65] R. Berman, P. R. W. Hudson, and M. Martinez, Nitrogen in diamond: Evidence from thermal conductivity, *J. Phys. C* **8**, L430 (1975).
- [66] C. A. Ratsifaritana and P. G. Klemens, Scattering of phonons by vacancies, *Int. J. Thermophys.* **8**, 737 (1987).
- [67] N. A. Katcho, J. Carrete, W. Li, and N. Mingo, Effect of nitrogen and vacancy defects on the thermal conductivity of diamond: An *ab initio* green's function approach, *Phys. Rev. B* **90**, 094117 (2014).
- [68] D. A. Broido, L. Lindsay, and A. Ward, Thermal conductivity of diamond under extreme pressure: A first-principles study, *Phys. Rev. B* **86**, 115203 (2012).
- [69] D. Spiteri, J. Anaya, and M. Kuball, The effects of grain size and grain boundary characteristics on the thermal conductivity of nanocrystalline diamond, *J. Appl. Phys.* **119**, 085102 (2016).